Geometrically nonlinear transient analyses of rotating structures through high-fidelity models

Composite Structures 343 (2024) 118265

Contents lists available at ScienceDirect

Composite Structures

journal homepage: www.elsevier.com/locate/compstruct

Geometrically nonlinear transient analyses of rotating structures through high-fidelity models

R. Azzara *, M. Filippi, E. Carrera

MUL^2*, Department of Mechanical and Aerospace Engineering Politecnico di Torino, Italy*

ARTICLE INFO

Keywords:
Finite element method
Carrera unified formulation
Higher-order models
Geometrical nonlinearity
Time response
Rotating structures

ABSTRACT

This work presents geometrically nonlinear transient analyses of various rotating blades. The structures are discretized through refined beams or multi-dimensional finite element models, which are generated using the Carrera Unified Formulation (CUF). The CUF offers a procedure to develop low- and high-fidelity one-dimensional, two-dimensional, and three-dimensional finite element models hierarchically and automatically. Various beam models were developed using different kinematics models based on Taylor or Lagrange expansion functions. Multi-dimensional models were obtained by merging beam and solid elements, exploiting the unique feature of Lagrange polynomials to have only pure displacements as unknowns. This property allows beam and solid elements to be coupled at the node level without requiring complicated mathematical formulations. By utilizing the Finite Element Method in conjunction with the CUF, the governing equations are written by including all rotation effects, namely the Coriolis term, spin-softening, and geometrical stiffening. In a total Lagrangian scenario, the Hilbert-Hughes-Taylor-α method and the iterative Newton-Raphson scheme are employed to solve the equations of motion. The proposed methodology has been applied to evaluate different blade configurations, comparing the solution obtained using linear, linearized, and nonlinear approaches. The results have been verified and validated by comparing them with existing solutions present in the literature.

1. Introduction

Rotating structures differ from non-rotating ones due to the coupling between rotating motion and elastic deformation caused by numerous forces acting on them. These forces can encompass, for example, aerodynamic loads and thermal gradients. The dynamic response of rotating structures to these forces can give rise to various issues, such as excessive vibrations, fatigue failure, resonance, and a shortened operational lifespan. Consequently, studying and predicting the dynamic characteristics of rotating structures are crucial for enhancing performance, improving reliability, and ensuring the safe and optimal operation of diverse machinery and equipment [1,2]. However, analyzing rotordynamics can become exceptionally challenging when nonlinear effects must be considered. Nonlinearities in rotor systems can stem from various factors [3], including large deformations, rotor-base excitations [4,5], geometrical nonlinearities [6], and magnetic bearings [7], among others.

The widespread adoption of the Finite Element Method (FEM) [8] has significantly influenced the field of rotordynamics. FEM allows for a detailed study of the dynamic behaviour of machines containing high-speed rotors, enabling quantitative predictions with significant accuracy. While the three-dimensional (3D) finite element approach is considered the most reliable, its computational cost often makes it impractical, especially during the preliminary design phase when multiple stress, dynamic, and aerodynamic analyses must be conducted. Therefore, the need for a comprehensive and computationally efficient tool for design activities justifies the adoption of lower-dimensional models, such as one-dimensional (1D) beams or two-dimensional (2D) plate/shell formulations. The traditional approach to modelling rotating blades and shafts typically involves beam models. Classical beam approaches, namely the Euler-Bernoulli and Timoshenko beam models, have been widely utilized in published literature. For example, Chung and Yoo [9] conducted finite element analyses of rotating cantilever Euler-Bernoulli beams, considering stretch deformation in dynamic modelling instead of axial deformation. Chung *et al.* [10] studied the flap motion of a cantilever beam with rotary oscillation caused by a harmonically varying rotating speed. Gao *et al.* [11] investigated the dynamics of Euler-Bernoulli beams under different rotating speeds and

* Corresponding author.
E-mail address: rodolfo.azzara@polito.it (R. Azzara).

https://doi.org/10.1016/j.compstruct.2024.118265
Received 26 March 2024; Received in revised form 31 May 2024; Accepted 5 June 2024
Available online 15 June 2024

acceleration, developing a sandwich structure to suppress vibration. Younesian and Esmailzadeh [12] examined the coupled axial-bending vibration of a viscoelastic Euler-Bernoulli beam and analyzed the effects of hub radius, structural damping, and acceleration rate on vibration amplitude. Young [13] explored coupled bending-bending vibrations of rotating pre-twisted, tapered beams with non-constant rotating speed. Hu *et al.* [14] presented accurate and efficient methodologies for predicting the dynamic response of various pre-twisted beam structures with varying rotating velocities. Du *et al.* [15] investigated transient analyses of rotating beam structures with a tip mass, while Park and Kim [16] studied the dynamic response of curved beams both with and without a tip mass. Pan and Liu [17] delved into geometrically nonlinear dynamic analyses of curved beams.

Even though classical beam models yield accurate results for many practical applications, they neglect factors such as cross-section deformations. Consequently, they may not be suitable for thin structures, composite blades, and non-classical boundary conditions, making their assumptions unacceptable in specific applications. In their works, Truong *et al.* [18] and Kang *et al.* [19] extensively discussed the reliability range of beam approaches. Researchers have explored the implementation of 2D formulations for modelling some rotating structures. Yao *et al.* [20] conducted nonlinear dynamic analyses of blades exposed to supersonic airflow with varying rotating speeds. Leissa [21,22] performed vibration analyses of turbine engine blades using shell theories. Hu *et al.* [23] analyzed the fundamental vibrations of rotating cantilever blades with pre-twist using a shell formulation. Kang *et al.* [19] assessed shell elements for modelling rotorcraft blades. More recently, Filippi *et al.* [24] employed high-fidelity shell formulations to analyze rotordynamics in various cylindrical and disk structures.

An alternative strategy to balance efficiency and accuracy when analyzing complex blade configurations involves developing multi-dimensional models that utilize solid elements for specific subdomains while employing mathematical models elsewhere. However, coupling different dimensional elements can introduce inconsistencies in the displacement and stress fields at the interface. Typically, classical beam models are adopted for this purpose, but compatibility conditions must be applied when integrating these elements with 3D finite elements (FEs) to ensure the continuity of displacement fields. To this end, various techniques, such as rigid body elements, transition elements, and variational coupling, have been devised. These methods yield satisfactory outcomes in terms of global displacements and natural frequencies, but they can provide inaccurate stress distributions at the interface level.

The primary goal of this research was to extend the dynamic investigation of complex rotating blade structures by incorporating geometrically nonlinearities through the utilization of multidimensional (3D/1D) models based on the Carrera Unified Formulation (CUF) [25]. The CUF enables the derivation of refined 1D, 2D, and 3D finite element models with variable kinematics. Taylor (TE) and Lagrange (LE) expansion functions are utilized to develop different kinematics models. In particular, the LE approach presents the advantage of having only pure displacements as unknowns, facilitating the coupling of beam and solid elements at the node level without necessitating complex mathematical formulations. Geometrical nonlinear equations are expressed using a total Lagrangian formulation and solved using a suitable Newton-Raphson method. The equations of motion are derived in a co-rotating frame of reference, accounting for all contributions due to the rotational speed, including the Coriolis and spin-softening effects. The Hilber-Hughes-Taylor (HHT)-α algorithm, formulated by Hilber *et al.* [26], is employed to solve the equations of motion.

Recent advancements in the field of CUF have primarily focused on nonlinear problems, showcasing its versatility and effectiveness. One notable accomplishment is the development of an efficient nonlinear beam model using CUF in conjunction with the asymptotic numerical method (ANN) [27,28]. Additionally, a highly effective and efficient framework, called multiscale CUF-FE2, has been created within the domain of classical homogenization method. This framework is particularly adept at solving geometric nonlinear problems, including the challenging task of addressing multiscale buckling problems [29]. The CUF-based model was built under the data-driven computational mechanics framework [30]. It integrates both Model-driven (MD) and Data-driven (DD) computing mechanics in the CUF domain for beam structures [31]. This approach uses DD CUF-based calculation for beam subdomains that present difficulties in obtaining accurate material constitutive models, such as areas affected by corrosion and microcracks. In contrast, MD CUF-based computation is used for the remaining subdomains where suitable constitutive models are available.

By employing the CUF, the computational cost of DD-MD CUF-based models can be significantly reduced compared to DD-MD FEM models that are based on solid elements, while maintaining an acceptable level of accuracy.

This paper is organized as follows: (i) Section 2 the nonlinear rotordynamics equations in the CUF formalism, focusing on the

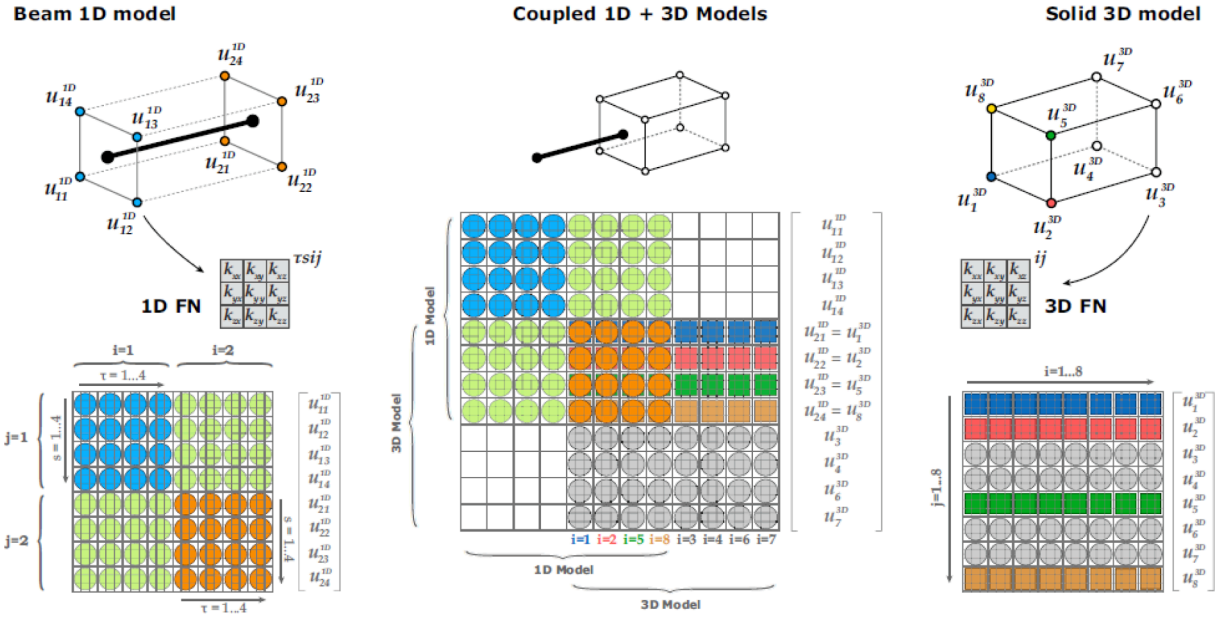

Fig. 1. Coupled 3D/1D models: assembling procedure.

development of refined beam and multi-dimensional models; (ii) Section 3 provides various numerical results to demonstrate the reliability of the proposed approach; (iii) Finally, Section 4 presents concluding remarks.

2. Rotordynamics equations in cuf form

2.1. CUF and FE approximation

According to the unified formulation and considering a Cartesian reference system (x, y, z), the 3D displacement field for beam and solid finite elements is defined as follows:

$$\begin{aligned} &Beam\,1D\ \ \boldsymbol{u}(x,y,z;t) = F_\tau(x,z)N_i(y)\boldsymbol{q}_{\tau i}(t) \quad \tau = 1,\ \cdots, M\ \ i = 1,\cdots,\ N_n^{1D} \\ &Solid\,3D\ \ \boldsymbol{u}(x,y,z;t) = 1{*}N_i(x,y,z)\boldsymbol{q}_{\tau i}(t) \quad\ \ i = 1,\cdots, N_n^{3D} \end{aligned} \tag{1}$$

in which F_τ stands for a set of functions of the cross-section for the beam, N_i represents the shape functions over the beam axis and solid volume, $\boldsymbol{q}_{\tau i}$ denotes the unknown nodal variables, M is the number of the expansion functions, N_n is the number of nodes per element, t indicates time and the repeated indexes stand for summation [25].

For beam elements, the class of the kinematic theory is determined by the choice of F_τ. Both Taylor expansion (TE) and Lagrange expansion (LE) functions can be adopted to approximate the displacement field. In particular, the utilization of LE models enables the independent assignment of a discretization for the displacement field to each subcomponent. This methodology is alternatively referred to as the Component-Wise (CW) approach [32]. By coupling the displacement fields of individual structural subcomponents, continuity of displacement is imposed at shared interfaces through nodal superposition, resulting in a straightforward coupling of finite element models. Lagrange polynomials are established within the natural reference system, exploiting the isoparametric formulation. In this work, LE are employed to easily generate multi-dimensional finite element models, i.e., merging beam and solid elements. In fact, the formulation takes advantage of a unique feature of this class of refined beam elements, which have only pure displacements as degrees of freedom. This property enables the connection of beam and solid elements by summing the elastic and inertial contributions of nodes that are shared by the two models. In detail, the nine-point (LE9) Lagrange polynomials and Taylor polynomials of various orders are adopted to formulate lower- and higher-order beam models, whereas the classical 1D FEs with four nodes (B4), i.e., quadratic approximation, are employed along the beam y-axis. For solid finite elements, the mathematical model is fully characterized by the total number of finite nodes involved, denoted as N_n^{3D}. Despite the fact that the basis of CUF expansion functions is set to $F_\tau = 1$, the unified approach still incorporates the definition of a 3D displacement field, which can be utilized effectively. In the following analyses, the quadratic hexahedral elements (HEXA27) are used for solid models. Fig. 1 illustrates an example of multi-dimensional model and the related assembling procedure. The assembly procedure is achieved by ensuring the equivalence of displacement components at corresponding nodes shared between two distinct models. When merging nodes of different finite element models, the Fundamental Nuclei (FNs) of stiffness matrices, introduced below, are superimposed and combined in the process of assembling global physical finite element matrices. The current approach is introduced as a solution to address the limitations of the existing variable-kinematics model found in commercial codes. In the proposed beam models, the kinematics of the cross-section is described using an independent 3D displacement field. Through the use of CUF, higher-order models can be easily derived without any loss of generality. This approach allows for the effective management of classical beam model restrictions, such as rigid cross-section, incompatibility between transverse normal and shear stresses at beam edges, and constant shear stress along the cross-section. Readers are referred to Refs. [33,34], which provide several illustrative examples of the implementation of multi-dimensional (3D/1D) models in the CUF domain. These examples pertain to the analysis of complex structures, encompassing static, vibration, and rotordynamics analyses.

The proposed nonlinear methodology is formulated adopting a total Lagrangian approach [35]. The Green-Lagrange strains are employed, and the displacement–strain relation and the constitutive law read:

$$\begin{aligned} &\boldsymbol{\varepsilon} = \boldsymbol{\varepsilon}_l + \boldsymbol{\varepsilon}_{nl} = (\boldsymbol{b}_l + \boldsymbol{b}_{nl})\boldsymbol{u} \\ &\boldsymbol{\sigma} = \boldsymbol{C}\boldsymbol{\varepsilon} \end{aligned} \tag{2}$$

where $\boldsymbol{b}_l$ and $\boldsymbol{b}_{nl}$ stand for the linear and nonlinear differential operators, respectively, and $\boldsymbol{C}$ is the material elastic matrix. The reader is referred to [8,36] for the complete expression of these matrices.

The principle of virtual work (PVW) is adopted to formulate the nonlinear FE equations.

$$\delta L_{int} + \delta L_{ine} - \delta L_{ext} = 0 \tag{3}$$

where δL_{int}, δL_{ine} and δL_{ext} indicate the virtual variation of the strain energy, inertial forces and external loadings, respectively. Their expressions are:

$$\begin{cases} \delta L_{int} = \delta \boldsymbol{q}_{sj}^{\mathrm{T}} \boldsymbol{K}_s^{ij\tau s} \boldsymbol{q}_{\tau i} \\ \delta L_{ine} = \delta \boldsymbol{q}_{sj}^{\mathrm{T}} \left(\boldsymbol{M}^{ij\tau s} \ddot{\boldsymbol{q}}_{\tau i} + \boldsymbol{G}^{ij\tau s} \dot{\boldsymbol{q}}_{\tau i} + \boldsymbol{K}_\Omega^{ij\tau s} q_{\tau i} + \boldsymbol{F}_\Omega^{sj} \right) \\ \delta L_{ext} = \delta \boldsymbol{q}_{sj}^{T} \boldsymbol{F}^{sj} \end{cases} \tag{4}$$

in which $\boldsymbol{K}_s^{ij\tau s}$, $\boldsymbol{M}^{ij\tau s}$,$\boldsymbol{G}^{ij\tau s}$, $\boldsymbol{K}_\Omega^{ij\tau s}$, $\boldsymbol{F}_\Omega^{sj}$ and $\boldsymbol{F}^{sj}$ represent the Fundamental Nuclei (FNs) of the secant stiffness matrix, mass matrix, Coriolis matrix, spin-softening matrix, centrifugal load and external load [37]. The superposed dots stand for time differentiation.

For undamped problems and considering the mass matrix constant, the nonlinear dynamic equilibrium equations become:

$$\boldsymbol{M}\ddot{\boldsymbol{q}}(t) + \Omega \boldsymbol{G}\dot{\boldsymbol{q}}(t)(\boldsymbol{K}_s + \Omega^2 \boldsymbol{K}_\Omega + \dot{\Omega}\boldsymbol{K}_{\dot{\Omega}})q(t) = \Omega^2 \boldsymbol{F}_\Omega(t) + \dot{\Omega}\boldsymbol{F}_{\dot{\Omega}}(t) \tag{5}$$

where $\boldsymbol{M}$, $\boldsymbol{G}$, $\boldsymbol{K}_s$, $\boldsymbol{K}_\Omega$, $\boldsymbol{K}_{\dot{\Omega}}$, $\boldsymbol{F}_\Omega$ and $\boldsymbol{F}_{\dot{\Omega}}$ indicate the assembled finite element arrays of the final FE model, while Ω stands for the rotational speed.

Equation (5) is solved by adopting a time integration algorithm and a Newton-Raphson method. Therefore, the tangent stiffness matrix $\boldsymbol{K}_T$ is introduced by linearizing the nonlinear governing equations around non-trivial equilibrium states.

$$\begin{aligned} &\delta(\delta L_{int} + \delta L_{ine} - \delta L_{ext}) = \delta \boldsymbol{q}^T(\boldsymbol{K}_0 + \boldsymbol{K}_{T1})\delta \boldsymbol{q} + \delta \boldsymbol{q}^T \boldsymbol{K}_\sigma \delta \boldsymbol{q} + \delta \boldsymbol{q}^T \boldsymbol{M} \delta \boldsymbol{q} \\ &= \delta \boldsymbol{q}^T \boldsymbol{K}_T^{ij\tau s} \delta \boldsymbol{q}_{\tau i} + \delta \boldsymbol{q}_{sj}^T \boldsymbol{M}^{ij\tau s} \delta \ddot{\boldsymbol{q}}_{\tau i} \end{aligned} \tag{6}$$

where $\boldsymbol{K}_0$ denotes the linear component of $\boldsymbol{K}_T$, $\boldsymbol{K}_{T1} = 2\boldsymbol{K}_{lnl} + \boldsymbol{K}_{nll} + 2\boldsymbol{K}_{nlnl}$ are the nonlinear contributions and $\boldsymbol{K}_\sigma$ is the geometric stiffness. The linearization of the virtual variation of external work is equal to zero because conservative forces are considered.

In the case of small deformations, $\boldsymbol{K}_T$, is approximated as the sum of the linear stiffness matrix ($\boldsymbol{K}_0$) and the geometric (pre-stress) contribution ($\boldsymbol{K}_\sigma^*$).

$$\boldsymbol{K}_T \approx \boldsymbol{K}_0 + \lambda \boldsymbol{K}_\sigma^* \tag{7}$$

where λ is the progressively increasing load factor proportional to Ω^2. It is important to underline that, in this case, the $\boldsymbol{K}_\sigma^*$ matrix refers only to the linear contributions of stress ($\boldsymbol{\sigma}_{lin}$). This last approach is identified as a *linearized* approach in the following sections.

The numerical algorithm employed to perform nonlinear transient analyses of rotating structures is reported in Appendix A.

3. Numerical examples

This section aims to assess the accuracy and effectiveness of the

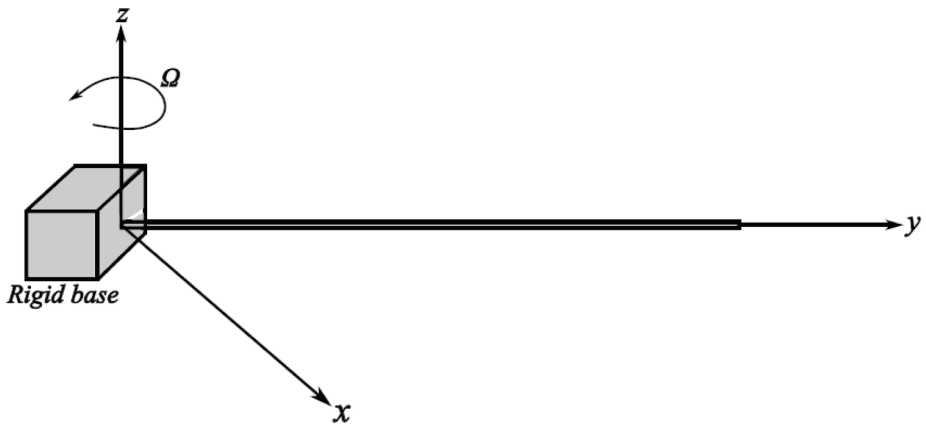

Fig. 2. Rotating cantilever beam.

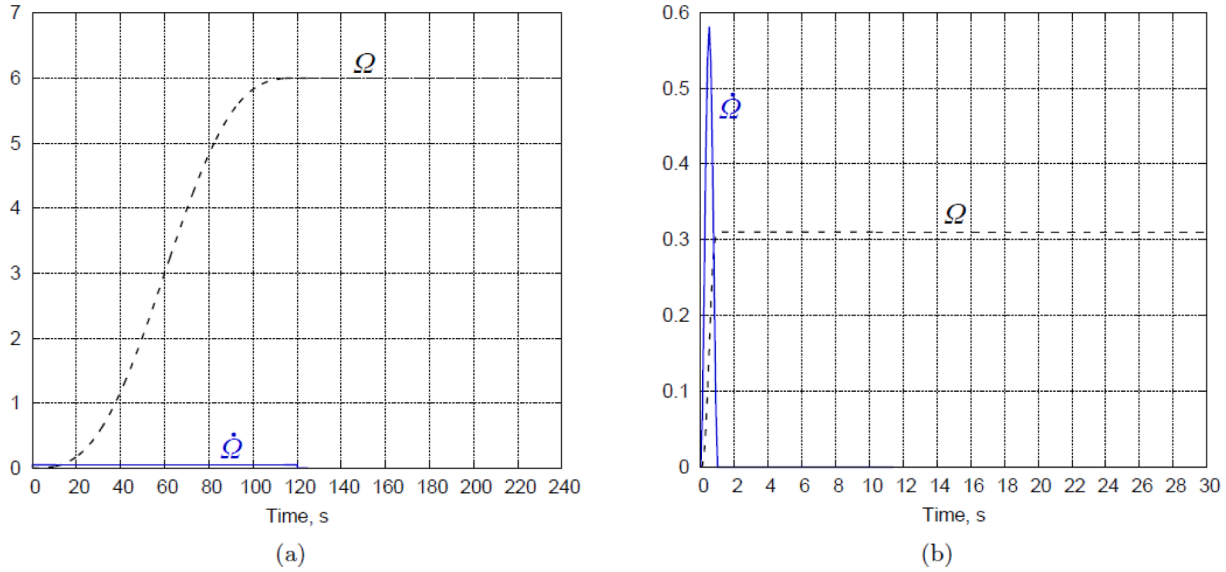

Fig. 3. (a) Smooth planar spin-up motion; (b) Abrupt planar spin-up motion.

proposed nonlinear dynamic formulation by evaluating various rotating structures under different speed profiles. The obtained results are compared with results found in the available literature. Linear, linearized, and nonlinear solutions are provided for all the examples examined. Moreover, convergence analyses were carried out for each case study, considering both the mesh approximation and time step size. For the first numerical case, a comparison between the LE solutions and those obtained using Taylor expansion (TE) functions of orders one (TE1) and two (TE2) is reported. Then, for subsequent cases, only higher-order LE and multi-dimensional models are utilized.

3.1. Cantilever beams

The first example concerned two cantilever beams attached to a rigid base, as depicted in Fig. 2. The base performs planar rotational motion around the z-axis according to various speed profiles. The structure is modelled by employing ten B4 along the longitudinal axis and adopting Taylor polynomials of various order or one LE9 over the beam cross-section.

The first case involves a smooth planar spin-up motion, in which he rotational speed is set to $\Omega_s = 6$ rad/s, and the parameter τ represents the normalized time $(\tau = t/T_s)$, with a time period of $T_s = 120$ s.

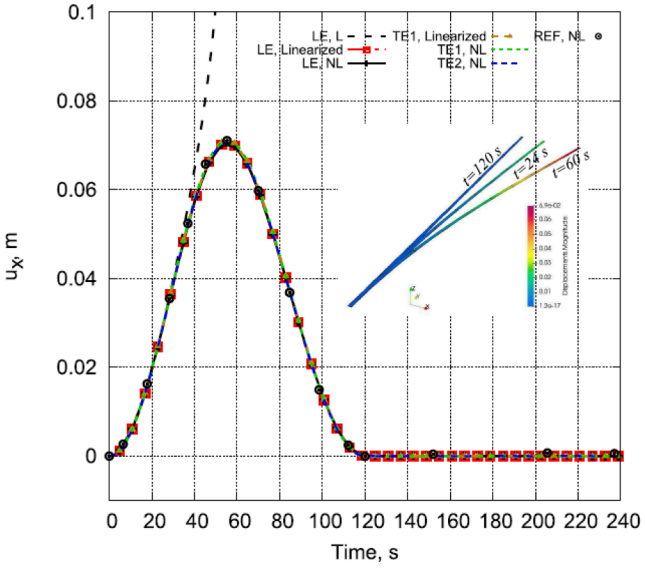

Fig. 4. Dynamic response at the tip of the beam subjected to a smooth planar spin-up motion.

Table 1
Lateral displacement (u_x) values as a function of the time at the tip of the beam subjected to a smooth planar spin-up motion. LE NL solution.

t [s]	$u_x[m]$
0.00	0.00
7.20	0.00273
14.40	0.01056
24.00	0.02690
31.20	0.04122
40.80	0.05862
46.80	0.06625
55.20	0.07053
66.00	0.06473
75.60	0.05193
84.00	0.03818
93.60	0.02263
102.00	0.01117
120.00	0.00

$$\Omega = \begin{cases} \Omega_s[\tau - \frac{1}{2\pi}\sin(2\pi\tau)] & if 0 \le \tau \le 1s \\ \Omega_s & if \tau > 1s \end{cases} \quad (8)$$

The structural configuration employed in this analysis was taken from Ref. [38]: length $L = 10$ m, cross-sectional area $A = 4.0 \times 10 - 4\ m^2$, moment of inertia $I = 2.0 \times 10 - 7\ m^4$, Young's modulus $E = 70$ GPa, density $\rho = 3000\ kg/m^3$. The time responses are calculated by assuming a time step dt equal to 1.2 s.

Fig. 3a plots the temporal evolutions of the rotational velocity and acceleration. In Fig. 4, the chordwise displacements at the tip of the beam are depicted, comparing the results obtained from linear (L), linearized, and nonlinear (NL) analyses using both Lagrange and Taylor expansion functions. The figure includes a reference solution and showcases various deformed configurations.

Furthermore, Table 1 reports the lateral displacement values at different times. In addition, Fig. 5 displays the stress distributions at the beam structure's root as a time function. Moreover, Fig. 6 provides the stress distribution along the entire axis of the beam for the analyzed time interval.

The results suggest that

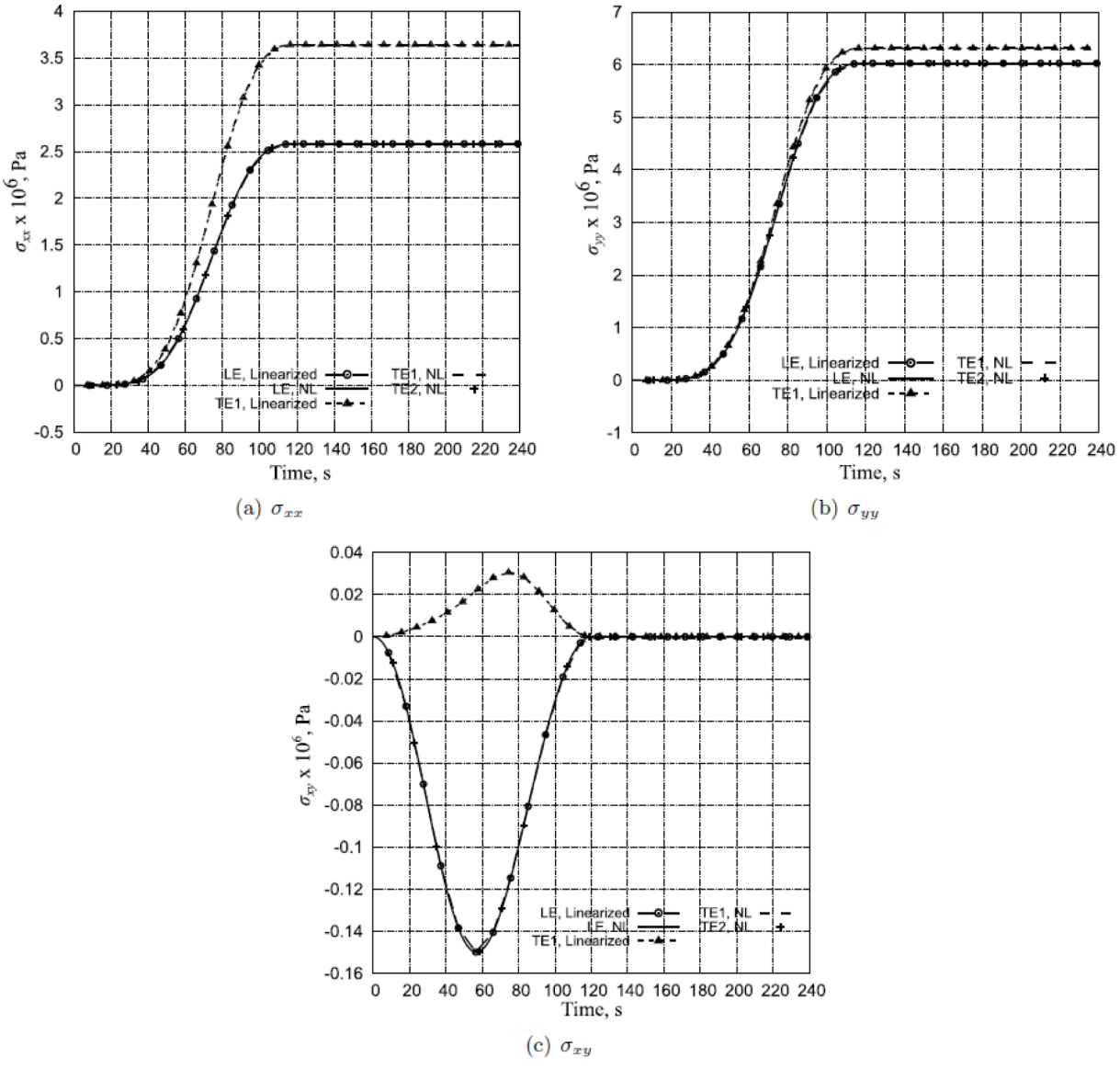

Fig. 5. Stress distributions versus time at the root of the beam subjected to a smooth planar spin-up motion.

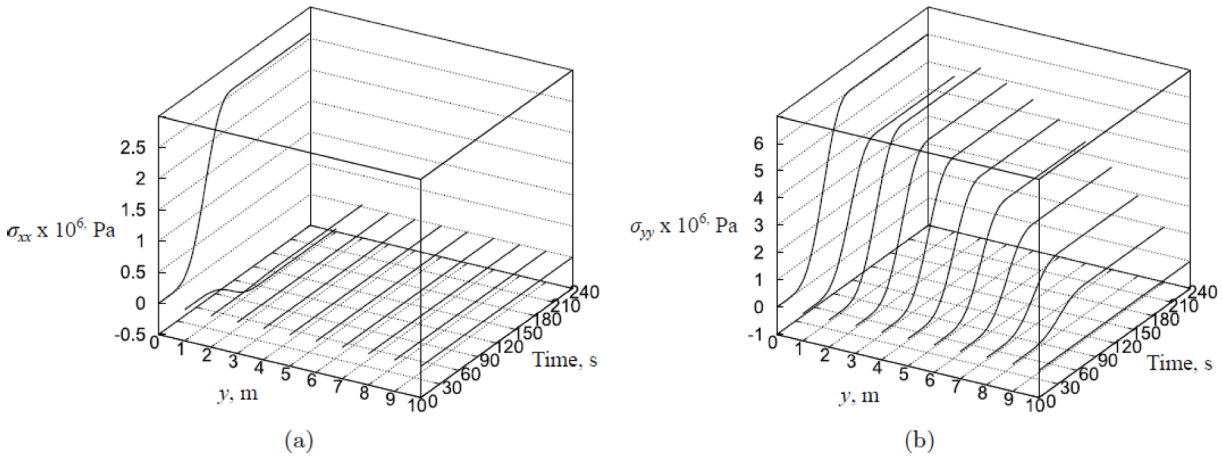

Fig. 6. 3D stress plots for the beam subjected to a smooth planar spin-up motion.

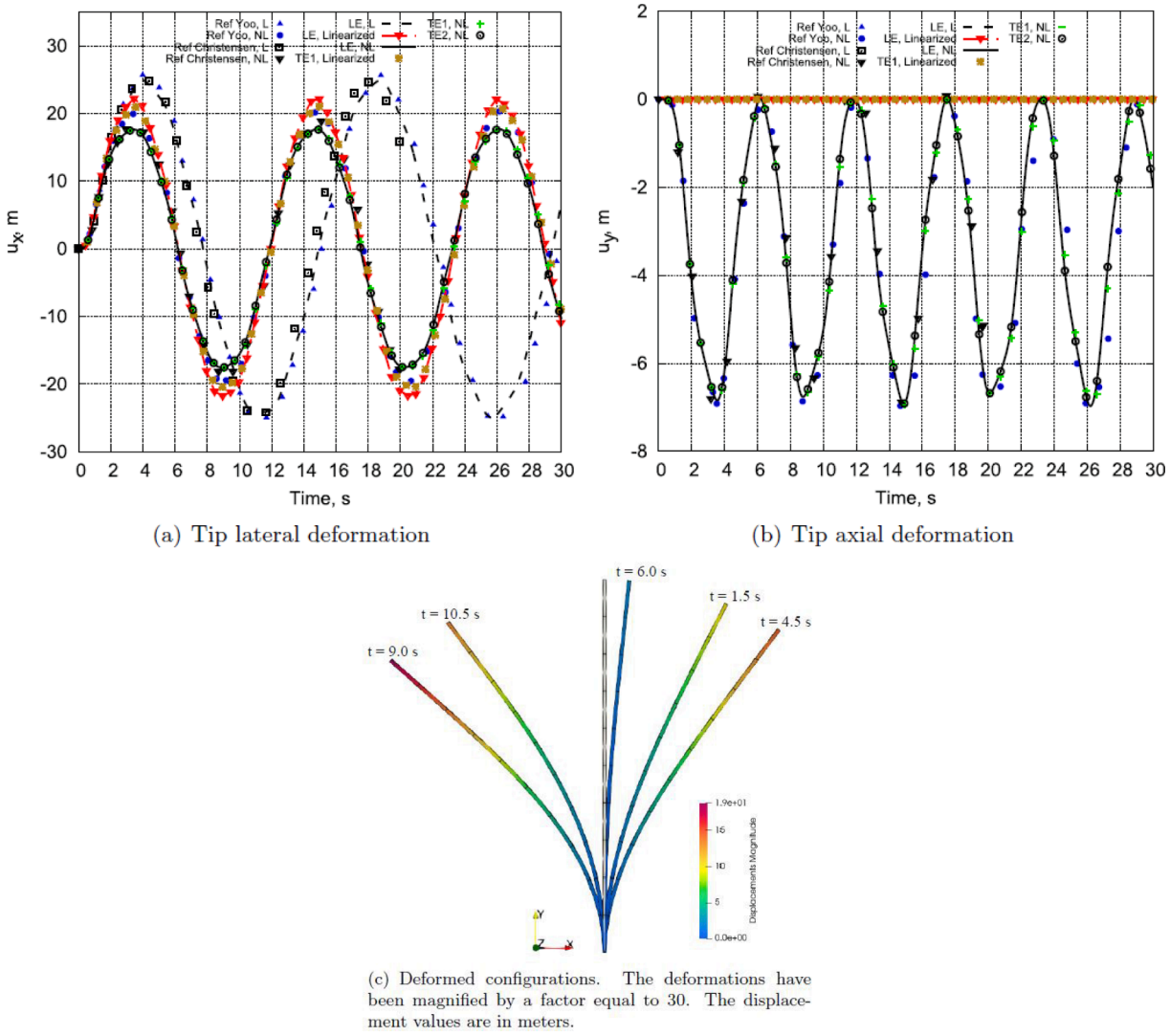

Fig. 7. Dynamic response of the beam subjected to an abrupt planar spin-up motion.

- After 40 s, the linear approach yields unreasonable results.
- The linearized formulation, adopting lower- (i.e., TE1) and higher-order (i.e., TE2, LE) models, provided the same response obtained with the nonlinear approach.
- The linearized and nonlinear solutions were in good agreement with the reference ones.
- The stress results for TE1 show variable differences compared to the LE and TE2 solutions. Significant discrepancies, close to 30 %, are

Table 2
Axial (u_y) and lateral (u_x) displacement values as a function of the time at the tip of the beam subjected to an abrupt planar spin-up motion. LE NL solution.

t [s]	$u_x[m]$	$u_y[m]$
0.00	0.00	0.00
1.50	9.923	−1.997
3.00	17.188	−6.247
4.50	14.297	−4.109
6.00	2.0332	−0.087
7.50	−11.923	−2.715
9.00	−17.540	−6.639
10.50	−12.861	−3.520
12.00	1.316	−0.032
15.00	17.509	−6.862
18.00	−5.235	−0.561
21.00	−16.639	−5.904
24.00	8.110	−1.107
27.00	15.361	−4.867
30.00	−10.377	−2.016

observed for σ_{xx}, while a relatively small percentage difference, less than 4 %, is obtained for σ_{yy}. Significant differences were also observed in the shear stress, σ_{xy}, distributions.

- The linearized TE2 and 1LE9 predictions significantly agreed with the nonlinear results.

Next, an abrupt planar spin-up motion is assumed. The data for this case were: $L = 30.5$ m, A.

$= 9.29 \times 10 - 2\ m^2$, $I = 7.19 \times 10 - 4\ m^4$, $E = 6.89$ GPa, $\rho = 2690.277$ kg$/m^3$. For this example, the prescribed base motion is given as:

$$\Omega = \begin{cases} \Omega_s[6\tau^5 - 15\tau^4 + 10\tau^3] & if 0 \le \tau \le 1s \\ \Omega_s & if \tau > 1s \end{cases} \quad (9)$$

where $\Omega_s = 0.31$ rad/s, $\tau = t/T_s$ with $T_s = 1$ s. The velocity and acceleration profiles are shown in Fig. 3b.

Fig. 7a and 7b illustrate the chordwise and axial displacements as functions of time ($dt = 0.05$ s). The linear, linearized, and nonlinear

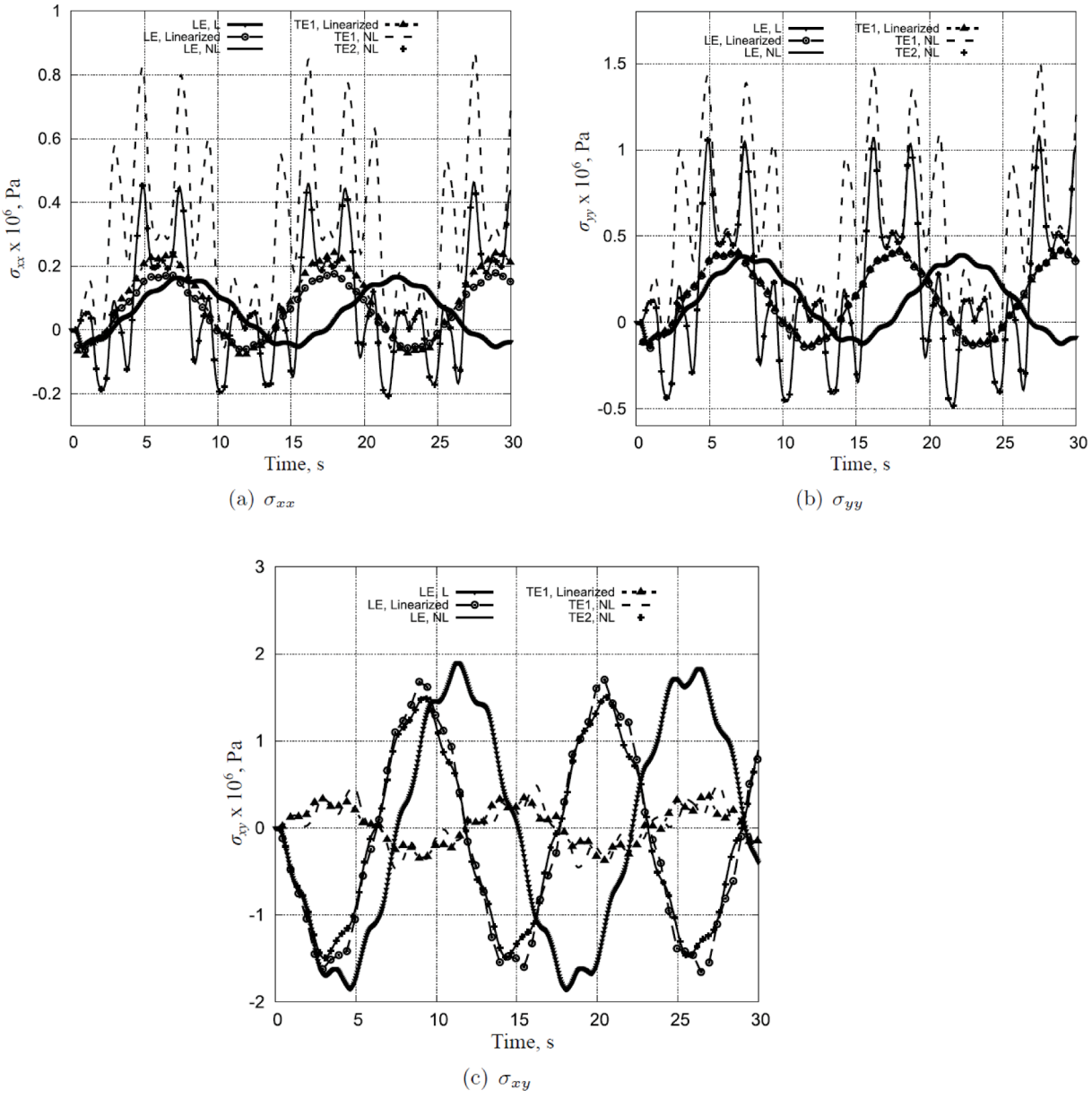

(a) σ_{xx} (b) σ_{yy}

(c) σ_{xy}

Fig. 8. Stress distributions versus time at the beam root subjected to an abrupt planar spin-up motion.

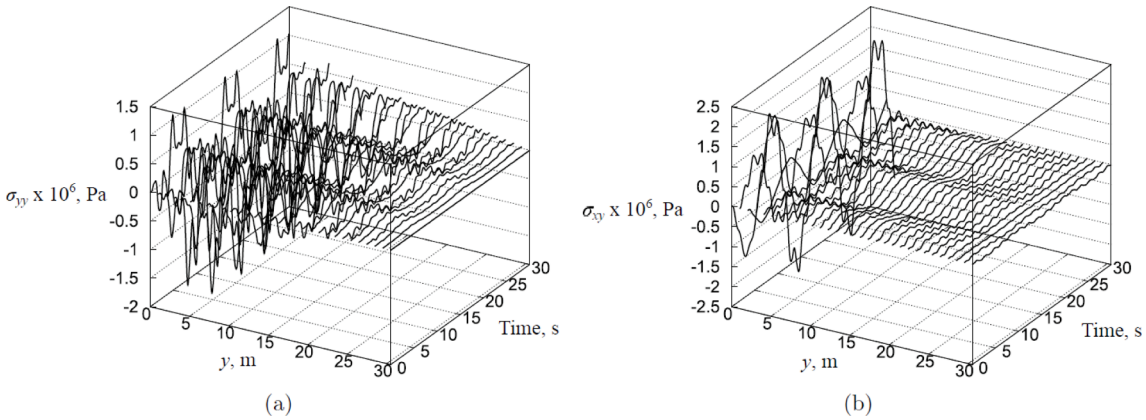

Fig. 9. 3D stress plots for the beam subjected to an abrupt planar spin-up motion.

results are compared with the solutions proposed by Yoo *et al.* [38] and by Christensen and Lee [39]. In addition, some deformed configurations at different times are shown in Fig. 7c. Table 2 provides the displacement values for different times.

Furthermore, Figs. 8 and 9 provide the 3D stress distributions at the root and over the entire axis of the beam structure, respectively.

The results suggest that

- Both linear and nonlinear CUF results show remarkable agreement with the reference solutions.
- The linear solutions differ from the nonlinear ones in amplitude and oscillation frequency. In particular, the linear approach led to larger chordwise deflection and did not capture the coupling between chordwise and axial deformations.
- The linearized approach provided a slightly larger lateral displacement, maintaining the same response period as the nonlinear solution. Nevertheless, the axial-bending coupling was not detected by the linearized models.
- The lower- (i.e., TE1) and higher-order (i.e., TE2, LE) models provided similar results with a percentage difference under 1 %.
- Significant differences were observed between the linear and nonlinear stress results using LE models. In particular, the linear approach underestimated the value of normal stresses, while slightly overestimated the shear ones.
- The linearized stress solutions maintain the same frequency oscillation as the nonlinear one, but different peaks are observed for the normal stress. At the same time, minor discrepancies can be observed in the shear stress plot.
- The TE1 model led to moderate discrepancies for normal stresses compared to LE solutions while providing inaccurate solutions for shear stresses.
- The nonlinear stresses provided by the TE2 model strongly agreed with the LE nonlinear predictions.

3.2. Swept-tip composite blade

The subsequent numerical application dealt with the dynamic response of a swept-tip composite blade. In this case, the fibre angle with respect to the y-axis, denoted by θ, was assumed equal to 0° for the straight portion and 45° for the tip. The geometric details, along with a schematic representation of the finite element model employed, are provided in Fig. 10. The material properties were: longitudinal modulus $E_L = 142$ GPa, transverse moduli $E_T = E_Z = 9.78$ GPa, shear moduli $G_{LT} = G_{LZ} = 6.14$ GPa, $G_{ZT} = 5.52$ GPa, Poisson's ratios $\nu_{LT} = \nu_{LZ} = 0.42$, $\nu_{LT} = 0.54$, density $\rho = 1538$ kg/m^3. The used mathematical model consisted of seven and five B4 beam elements along the straight portion and the tip of the blade, respectively. Two LE9 kinematic model has been adopted for the beam elements while 6 HEXA27 solid elements were utilized to discretize the transition zone. The model encompasses a total of 1935 degrees of freedom (DOFs).

The following speed profile has been selected, see Fig. 11a, in which the rotational speed is set to$\omega_z = 750$ rpm, and the parameter $\tau = t/T_s$, with $T_s = 1$ s. A time step of $dt = 0.05$ s was adopted for the subsequent dynamic analysis.

$$\Omega = \begin{cases} \frac{\omega_z}{10}(t - \frac{5}{\pi} sin\frac{\pi t}{5}) if 0 \le \tau \le 10s \\ \omega_z if 10 < \tau < 40s \\ \frac{\omega_z}{10}(50 - t + \frac{5}{\pi} sin\frac{\pi t}{5}) if 40 \le \tau \le 50s \end{cases} \quad (10)$$

Fig. 12 illustrates the response in terms of displacements of two points (denoted as A and B) obtained using the linear, linearized, and nonlinear approaches. The reference solution, taken from Ref. [33], coincides with the linearized approach proposed in this work. Some deformed configurations are depicted in Fig. 11b. Furthermore, Table 3 reports displacement values for different times, and Fig. 13 provides the 3D stress distributions as functions of time at the root of the blade.

The results suggest that

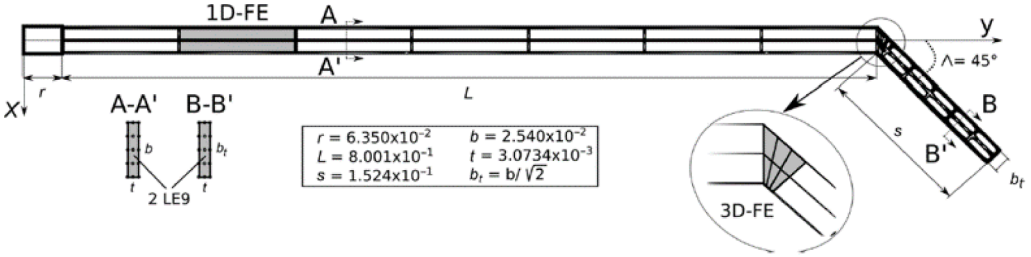

Fig. 10. Rotating swept-tip composite blade.

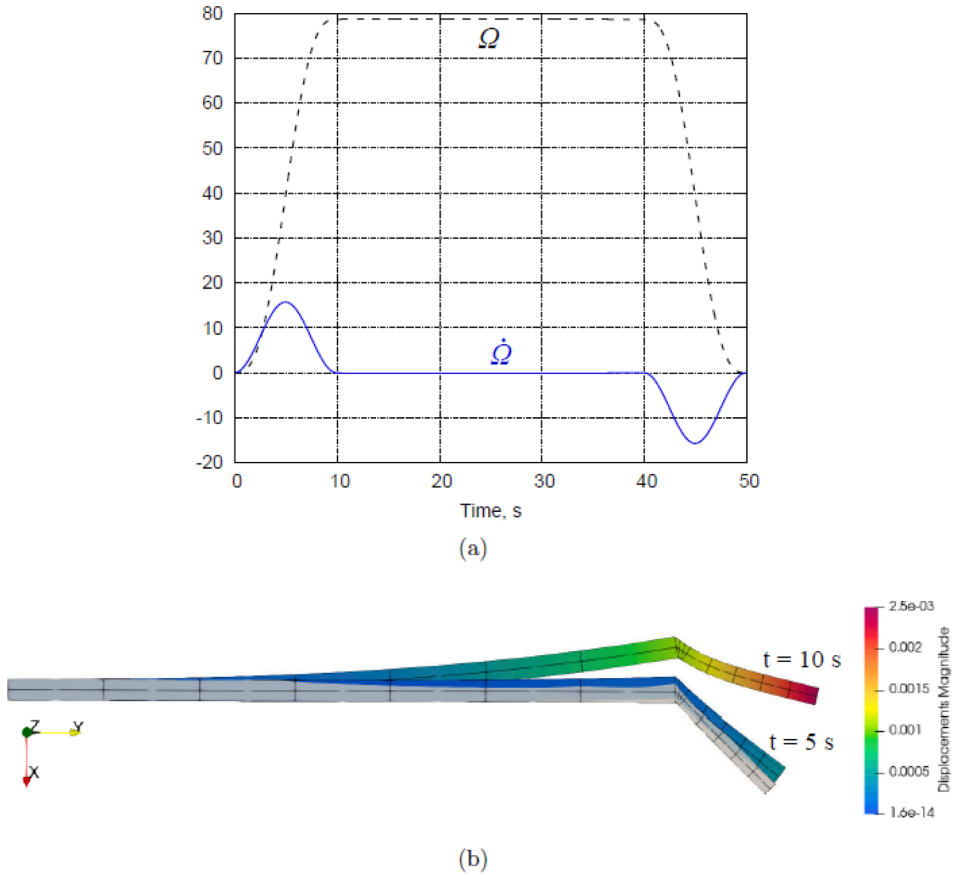

Fig. 11. (a) Rotating speed and acceleration profiles; (b) Deformed configurations of the swept-tip composite blade. The deformations have been magnified by a factor equal to 50. The displacement values are in meters.

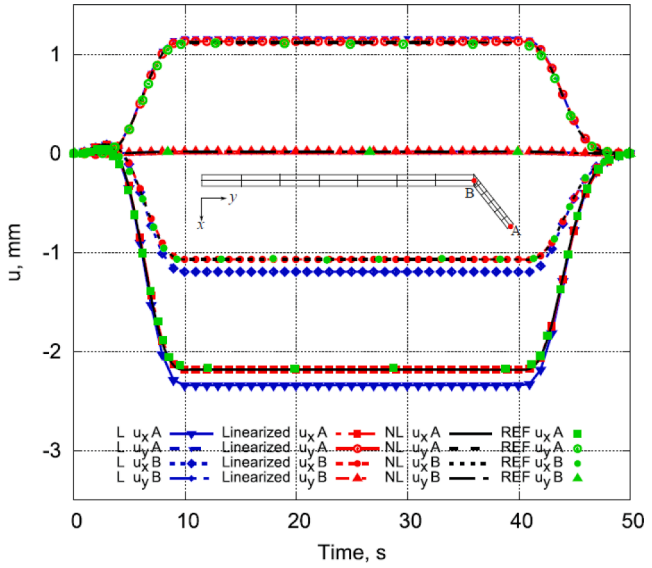

Fig. 12. Dynamic response at points A and B of the swept-tip composite blade.

- The nonlinear results exhibited remarkable agreement with the reference solution, whereas certain discrepancies can be observed with the linear ones. Compared to the nonlinear predictions, the linear approach overestimated the deflection in the x-direction whilst providing similar results in the y-direction.
- The linearized solutions reproduced the nonlinear predictions.

Table 3
Displacement values as a function of the time at points A and B of the swept-tip composite blade. NL solution.

t [s]	POINT A		POINT B	
	$u_x[mm]$	$u_y[mm]$	$u_x[m]$	$u_y[mm]$
0.00	0.00	0.00	0.00	0.00
5.00	−0.3712	0.2592	−0.1162	0.0045
10.00	−2.1851	1.1190	−1.0717	0.0163
25.00	−2.1851	1.1190	−1.0717	0.0163
40.00	−2.1845	1.1188	−1.0712	0.0163
45.00	−0.7383	0.3092	−0.4324	0.0040
50.00	0.00	0.00	0.00	0.00

- All the approaches agreed on computing normal stresses, while slight discrepancies between linear, linearized, and nonlinear solutions can be noted in the shear stress plot. In detail, the linear solution overestimated the nonlinear one, whereas the linearized one underestimated it.

3.3. NACA double-swept rotor blade

The last case concerned a rotor blade with a realistic airfoil. Fig. 14 shows the adopted finite element model and the dimensions. The discretization of the blade involved the utilization of eight B4 and nineteen LE9 elements for the beam portion and 152 HEXA27 elements for the transition zones.

The resulting model consisted of 13,200 DOFs. The metallic skin and foam had the following properties: Young's modulus of the metallic skin $E_m = 72.4$ GPa, Poisson's ratio $\nu_m = 0.3$, density $\rho_m = 2700$ kg/m^3, Young's modulus of the foam $E_f = 2.7$ GPa, Poisson's ratio $\nu_f = 0.22$ and

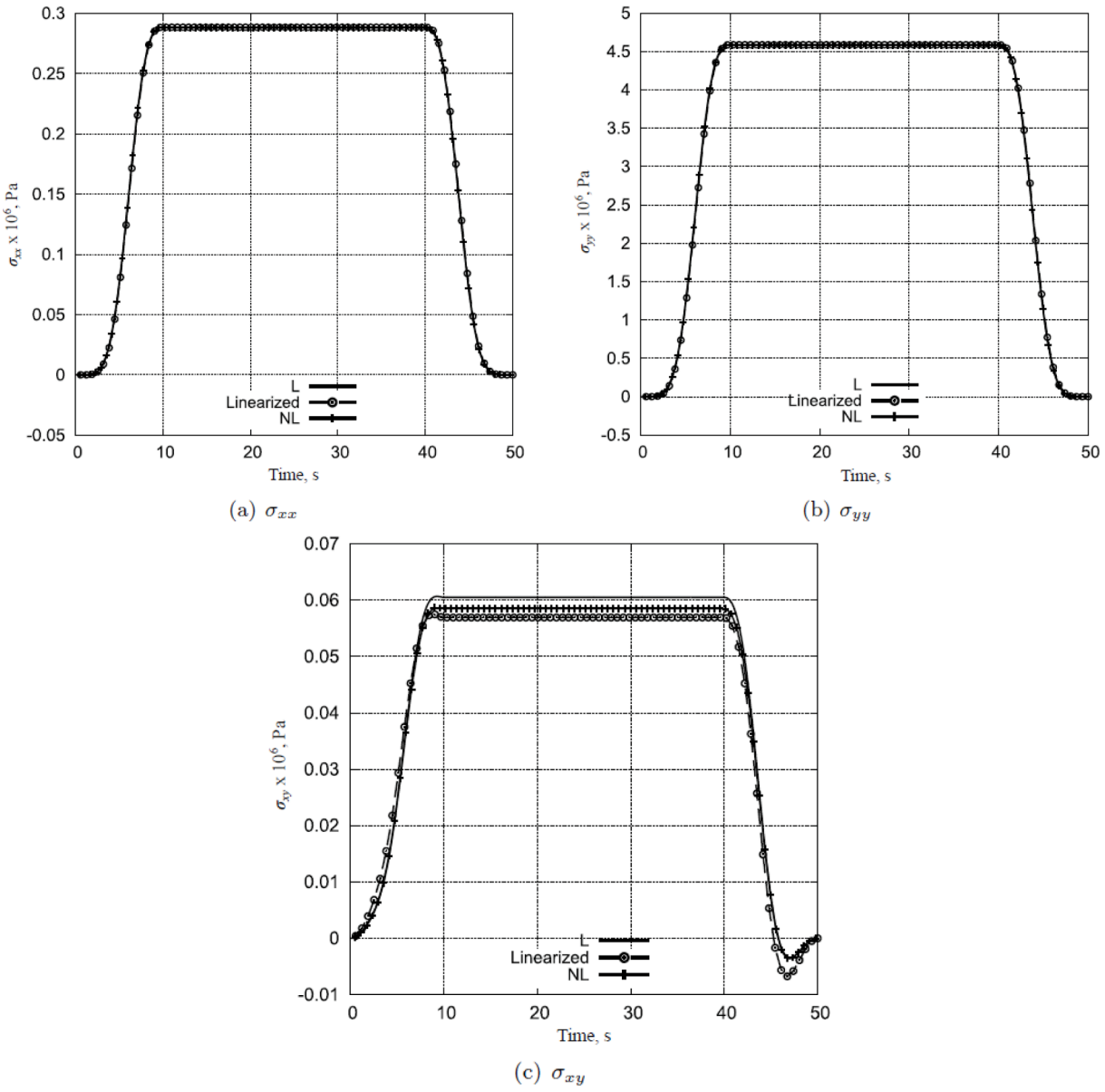

Fig. 13. Stress distributions versus time at the root of the swept-tip composite blade.

density $\rho_f = 200$ kg/m^3. A rigid hub length of 1 m was considered, and the analysis were performed selecting a time step $dt = 0.05$. The following speed profile was employed:

$$\Omega = \begin{cases} \frac{\omega_z}{10}(t - \frac{5}{\pi} sin\frac{\pi t}{5}) if 0 \leq \tau \leq 10s \\ \omega_z if 10 < \tau < 40s \\ \frac{\omega_z}{10}(50 - t + \frac{5}{\pi} sin\frac{\pi t}{5}) if 40 \leq \tau \leq 50s \end{cases} \quad (11)$$

with $\omega_z = 350$ rpm, see Fig. 15.

The obtained results are plotted in Fig. 16 in terms of displacements at point T. Additionally, the displacement values for different times are tabulated in Table 4. Furthermore, Fig. 17 provides the stress distributions as a function of the time at the two different points, C and P, see Fig. 15.

The results suggest that

- The linear approach provided a large deflection of the blade.
- The linearized solution exhibited good agreement with the nonlinear one for the chordwise displacement, while some discrepancies can be observed for the axial deformation. Compared to the nonlinear solution, the linearized approach overestimated the displacement u_y by about 1.3 cm.
- The linearized and nonlinear stress solutions perfectly agreed, except for the shear stress σ_{xy} calculated at point P, where slight discrepancies can be distinguished. However, this stress value presented two orders of magnitude lower than other stresses.

4. Conclusions

The present paper presented geometrically nonlinear transient analyses of various rotating structures using high-fidelity models. The blades were modelled utilizing either one-dimensional models or multi-dimensional models obtained with the Carrera Unified Formulation. Taylor and Lagrange expansions were employed to determine the class of kinematics theories and establish a connection between the beam and solid models. The geometrical nonlinear equations were expressed using a total Lagrangian formulation and solved with a Newton-Raphson

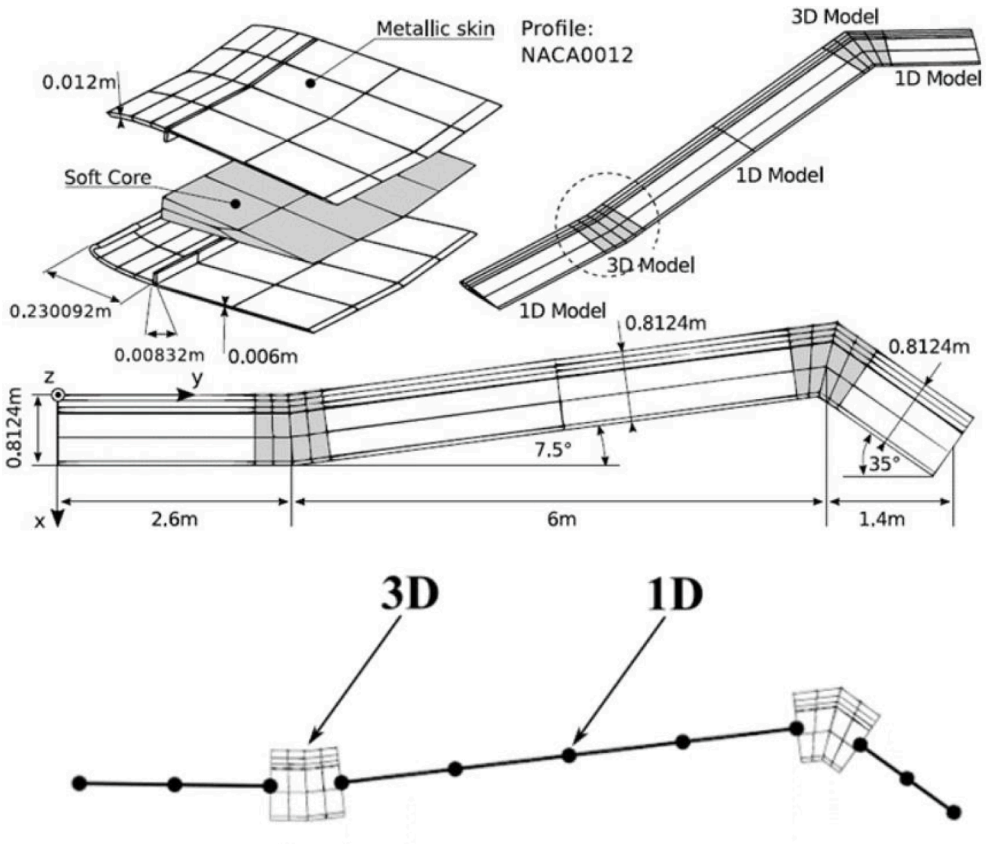

Fig. 14. Reference frame, geometry and beam-solid connection of the NACA double-swept blade.

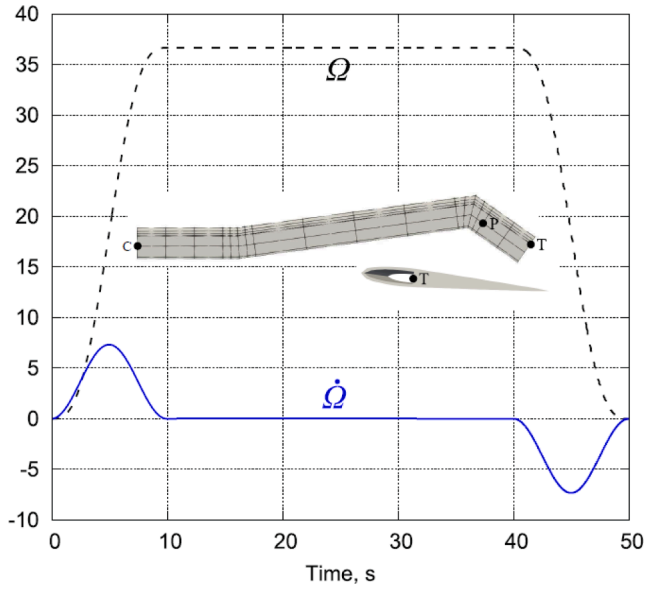

Fig. 15. Rotating speed and acceleration profiles.

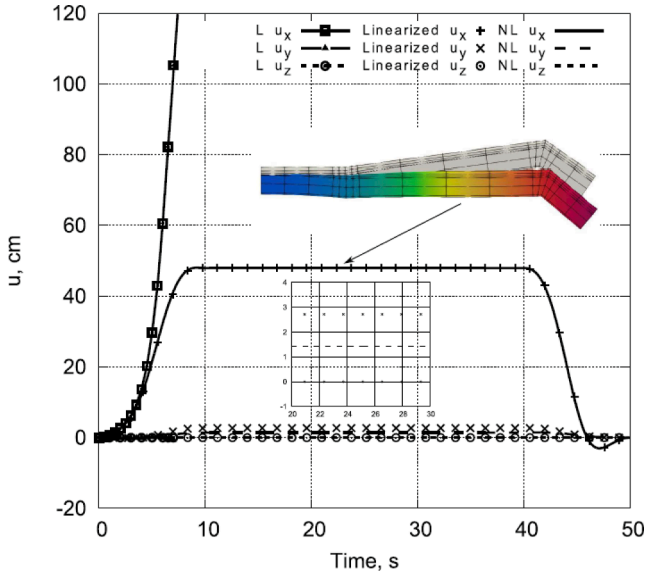

Fig. 16. Displacements history at the point T of the NACA double-swept blade. The deformation of the configuration shown has been magnified by a factor of 2.

method in conjunction with the Hilber-Hughes-Taylor-α time integration scheme. The equations of motion were derived with respect to a co-rotating frame of reference, including all contributions due to the rotational speed, namely the Coriolis and spin-softening terms. The results were compared with published solutions to validate the proposed approach. The following conclusions can be drawn:

- The present approach proved reliable for various blade configurations, namely a cantilever beam, swept-tip composite blade and NACA double-swept rotor blade.
- The classical linear interpolation provided by the first-order Taylor expansion presented similar results for displacements compared to higher-order solutions, while different stress distributions have been observed.

Table 4
Displacements as a function of the time at point T of the NACA double-swept blade. NL solution.

t [s]	$u_x[m]$	$u_y[mm]$
0.00	0.00	0.00
2.50	0.0407	−0.0009
5.00	0.2162	0.0016
7.50	0.4442	0.0103
10.00	0.4798	0.0142
25.00	0.4798	0.0142
40.00	0.4798	0.0142
45.00	0.0803	0.0072
48.00	−0.0211	0.0007
50.00	0.00	0.00

- A nonlinear approach was required to accurately evaluate the dynamic response of rotating blades subjected to abrupt acceleration manoeuvres. In contrast, a linearized methodology was accurate enough for smooth manoeuvres.

Finally, this method provides reasonable confidence for future applications in this topic. In particular, future works will concern the introduction of aerodynamic and thermal loads.

CRediT authorship contribution statement

R. Azzara: Writing – original draft, Visualization, Investigation. **M. Filippi:** Writing – review & editing, Supervision, Software. **E. Carrera:** Methodology, Funding acquisition, Conceptualization.

Declaration of competing interest

The authors declare that they have no known competing financial interests or personal relationships that could have appeared to influence the work reported in this paper.

Data availability

No data was used for the research described in the article.

Appendix A

A Nonlinear dynamic formulation

Considering the values known at the time t, the corresponding ones at $t + \Delta t$ are calculated using the HHT-α method, in which the equation of motion is expressed as follows:

$$\boldsymbol{M}\ddot{\boldsymbol{q}}_{t+\Delta t} + (1+\alpha)\Omega\boldsymbol{G}\dot{\boldsymbol{q}}_{t+\Delta t} - \alpha\Omega\boldsymbol{G}\dot{\boldsymbol{q}}_t + (1+\alpha)(\boldsymbol{K} + \Omega^2\boldsymbol{K}_\Omega + \dot{\Omega}\boldsymbol{K}_{\dot{\Omega}})\boldsymbol{q}_{t+\Delta t} - \alpha(\boldsymbol{K} + \Omega^2\boldsymbol{K}_\Omega + \dot{\Omega}\boldsymbol{K}_{\dot{\Omega}})\boldsymbol{q}_t = (1+\alpha)\Omega^2\boldsymbol{F}_{\Omega_{t+\Delta t}} - \alpha\Omega^2\boldsymbol{F}_{\Omega_t} + (1+\alpha)\dot{\Omega}\boldsymbol{F}_{\dot{\Omega}_{t+\Delta t}} - \alpha\dot{\Omega}\boldsymbol{F}_{\dot{\Omega}_t} \tag{12}$$

In order to obtain approximate step-by-step solutions of Eq. (12), the classical Newmark assumptions for velocities and displacements within the time step Δt are introduced.

$$\begin{aligned}\dot{\boldsymbol{q}}_{t+\Delta t} &= \dot{\boldsymbol{q}}_t + [(1-\gamma)\ddot{\boldsymbol{q}}_t + \gamma\ddot{\boldsymbol{q}}_{t+\Delta t}]\Delta t \\ \boldsymbol{q}_{t+\Delta t} &= \boldsymbol{q}_t + \dot{\boldsymbol{q}}_t\Delta t + [(\frac{1}{2}-\beta)\ddot{\boldsymbol{q}}_t + \beta\ddot{\boldsymbol{q}}_{t+\Delta t}]\Delta t^2\end{aligned} \tag{13}$$

where $\beta = (1-\alpha)2/4$ and $\gamma = (1-2\alpha)/2$. The parameters α, β and γ control the accuracy, stability, and numerical dissipation characteristics. As described by Hilber *et al.* [26], to use adequate numerical damping properties in the higher modes while at the same time ensuring that the lower modes are not affected too strongly, a value of $-1/3 \leq \alpha \leq 0$ has to be employed.

The resolution of the numerical algorithm employed for conducting nonlinear dynamic analyses of rotating structures can be outlined through the following steps:

1. Form stiffness $\boldsymbol{K}$, mass matrix $\boldsymbol{M}$, Coriolis Matrix $\boldsymbol{G}$ and spin-softening matrix $\boldsymbol{K}_\Omega$;
2. $\boldsymbol{K}_\Omega = \frac{1}{2}\boldsymbol{G}$;
3. Set the initial conditions;
4. For each time step:

(a) Starting condition:

$$\begin{cases} \ddot{\boldsymbol{q}}_{t+\Delta t} = 0 \\ \boldsymbol{q}_{t+\Delta t} = \boldsymbol{q}_t + \dot{\boldsymbol{q}}_t\Delta t + \ddot{\boldsymbol{q}}_t(1/2-\beta)\delta^2 + \ddot{\boldsymbol{q}}_{t+\Delta t}\beta\Delta t^2 \\ \dot{\boldsymbol{q}}_{t+\Delta t} = \dot{\boldsymbol{q}}_t + \ddot{\boldsymbol{q}}_t(1-\gamma)\Delta + \ddot{\boldsymbol{q}}_{t+\Delta t}\gamma\Delta t \end{cases} \tag{14}$$

(b) Form residual load vector $\boldsymbol{R}_{t+\Delta t}$:

$$\boldsymbol{R}_{t+\Delta t} = (1+\alpha)\Omega^2\boldsymbol{F}_{\Omega_{t+\Delta t}} - \alpha\Omega^2\boldsymbol{F}_{\Omega_t} + (1+\alpha)\dot{\Omega}\boldsymbol{F}_{\dot{\Omega}_{t+\Delta t}} - \alpha\dot{\Omega}\boldsymbol{F}_{\dot{\Omega}_t} - (1+\alpha)\boldsymbol{r}_{t+\Delta t} + \alpha\boldsymbol{r}_t - \boldsymbol{M}\ddot{\boldsymbol{q}}_{t+\Delta t} \tag{15}$$

in which $\boldsymbol{r}$ represents the contribution of the internal force and of the residue due to the

$\boldsymbol{K}_{\dot{\Omega}}, \boldsymbol{K}_\Omega, \boldsymbol{G}$.

(c) Newton-Raphson iteration convergence:
i. while $||\boldsymbol{R}_{t+\Delta t}|| \geq Tol$ **do**.

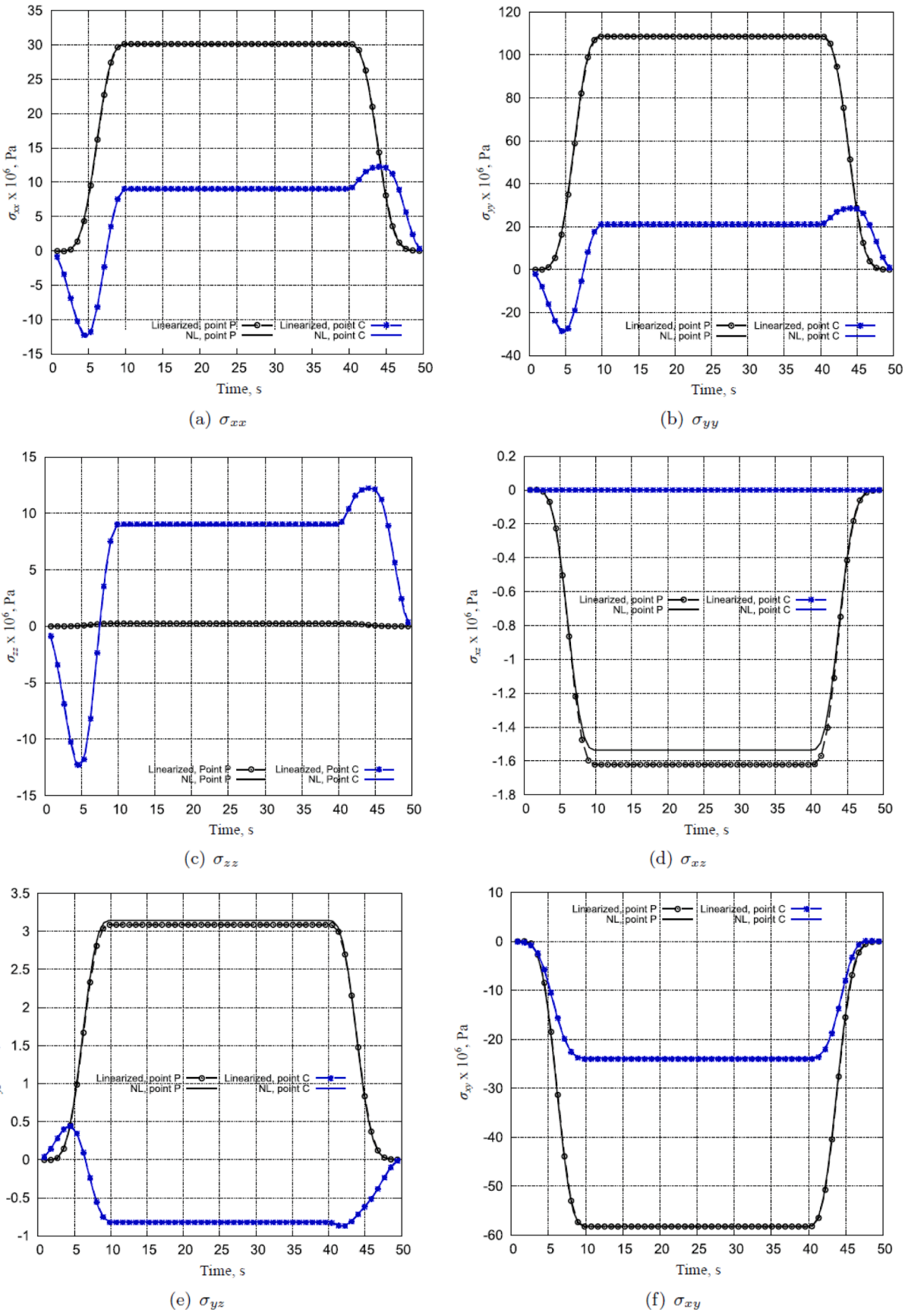

Fig. 17. Stress distributions versus time at points C and P of the NACA double-swept blade.

ii. Calculate tangent stiffness matrix $\boldsymbol{K}_T$;
iii. Solve for incremental acceleration $\Delta\ddot{\boldsymbol{q}}_{t+\Delta t}$;

$$[(\boldsymbol{M}+\Omega\boldsymbol{G}\gamma\Delta t(1+\alpha)+\boldsymbol{K}_T\beta\Delta t^2(1+\alpha)]\Delta\ddot{\boldsymbol{q}}_{t+\Delta t}=\boldsymbol{R}_{t+\Delta t} \tag{16}$$

iv Calculate new acceleration, velocity and displacement vectors:

$$\begin{cases}\ddot{q}_{t+\Delta t}=\ddot{q}_{t+\Delta t}+\Delta\ddot{q}_{t+\Delta t}\\ \dot{q}_{t+\Delta t}=\dot{q}_{t+\Delta t}+\Delta\dot{q}_{t+\Delta t}\\ q_{t+\Delta t}=q_{t+\Delta t}+\Delta q_{t+\Delta t}\end{cases} \tag{17}$$

v Calculate new residual load vector.

$$\boldsymbol{R}_{t+\Delta t}=(1+\alpha)\Omega^2\boldsymbol{F}_{\Omega_{t+\Delta t}}-\alpha\Omega^2\boldsymbol{F}_{\Omega_t}+(1+\alpha)\dot{\Omega}\boldsymbol{F}_{\dot{\Omega}_{t+\Delta t}}-\alpha\dot{\Omega}\boldsymbol{F}_{\dot{\Omega}_t}-(1+\alpha)\boldsymbol{r}_{t+\Delta t}+\alpha\boldsymbol{r}_t-\boldsymbol{M}\ddot{\boldsymbol{q}}_{t+\Delta t} \tag{18}$$

vi end while
(d) Next time step.

References

[1] Genta G. Dynamics of rotating systems. New York: Springer Science & Business Media; 2005.
[2] Adams ML. Rotating machinery vibration: from analysis to troubleshooting. New York: Dekker; 2009.
[3] Ehrich FF. Observations of nonlinear phenomena in rotordynamics. J Syst Des Dyn 2008;2(3):641–51.
[4] Driot N, Lamarque CH, Berlioz A. Theoretical and experimental analysis of a base excited rotor. ASME J Computat Nonlinear Dyn 2006;1(4):257–63.
[5] Duchemin M, Berlioz A, Ferraris G. Dynamic behavior and stability of a rotor under base excitation. J Vib Acoust 2006;128(5):576–85.
[6] Luczko J. A geometrically non-linear model of rotating shafts with internal resonance and self-excited vibration. J Sound Vib 2002;255(3):433–56.
[7] Ji JC, Leung AYT. Non-linear oscillations of a rotor-magnetic bearing system under superharmonic resonance conditions. Int J Non Linear Mech 2003;38(6):829–35.
[8] Bathe KJ. Finite element procedure. Upper Saddle River, New Jersey, USA: Prentice Hall; 1996.
[9] Chung J, Yoo HH. Dynamic analysis of a rotating cantilever beam by using the finite element method. J Sound Vib 2002;249(1):147–64.
[10] Chung J, Jung D, Yoo HH. Stability analysis for the flapwise motion of a cantilever beam with rotary oscillation. J Sound Vib 2004;273(4–5):1047–62.
[11] Gao K, Gao W, Wu D, Song C. Nonlinear dynamic stability analysis of Euler-Bernoulli beam–columns with damping effects under thermal environment. Nonlinear Dyn 2017;90:2423–44.
[12] Younesian D, Esmailzadeh E. Non-linear vibration of variable speed rotating viscoelastic beams. Nonlinear Dyn 2010;60:193–205.
[13] Young TH. Dynamic response of a pretwisted, tapered beam with non-constant rotating speed. J Sound Vib 1991;150(3):435–46.
[14] Hu Y, Zhao Y, Wang N, Chen X. Dynamic analysis of varying speed rotating pretwisted structures using refined beam theories. Int J Solids Struct 2020;185:292–310.
[15] Du X, Zhang J, Guo X, Li L, Zhang D. Dynamics analysis of rotating cantilever beams with free end mass. Appl Sci 2022;12(15):7553.
[16] Park JH, Kim JH. Dynamic analysis of rotating curved beam with a tip mass. J Sound Vib 1999;228(5):1017–34.
[17] Pan KQ, Liu JY. Geometric nonlinear dynamic analysis of curved beams using curved beam element. Acta Mechanica Sinica 2011;27(6):1023–33.
[18] Truong KV, Yeo H, Ormiston RA. Structural dynamics modeling of rectangular rotor blades. Aerosp Sci Technol 2013;30(1):293–305.
[19] Kang H, Chang C, Saberi H, Ormiston RA. Assessment of beam and shell elements for modeling rotorcraft blades. J Aircr 2014;51(2):520–31.
[20] Yao M, Ma L, Zhang W. Nonlinear dynamics of the high-speed rotating plate. Int J Aerospace Eng 2018;1–23:2018.
[21] Leissa AW. Vibrations of turbine engine blades by shell analysis. Shock Vib Dig 1980;12(11):3–10.
[22] Leissa AW, Lee JK, Wang AJ. Rotating blade vibration analysis using shells. ASME J Eng Power 1982;104(2):296–302.
[23] Hu XX, Sakiyama T, Matsuda H, Morita C. Fundamental vibration of rotating cantilever blades with pre-twist. J Sound Vib 2004;271(1–2):47–66.
[24] Filippi M, Azzara R, Carrera E. Rotordynamic analyses with variable-kinematic beam and shell finite elements. Mech Adv Mater Struct pages 1–13, 2023.
[25] Carrera E, Cinefra M, Petrolo M, Zappino E. Finite element analysis of structures through unified formulation. John Wiley & Sons, Chichester, West Sussex, UK; 2014.
[26] Hilber HM, Hughes TJR, Taylor RL. Improved numerical dissipation for time integration algorithms in structural dynamics. Earthq Eng Struct Dyn 1977;5(3):283–92.
[27] Hui Y, Giunta G, De Pietro G, Belouettar S, Carrera E, Huang Q, et al. A geometrically nonlinear analysis through hierarchical one-dimensional modelling of sandwich beam structures. Acta Mechanica 2023;234(1):67–83.
[28] Hui Y, Huang Q, De Pietro G, Giunta G, Hu H, Belouettar S, et al. Hierarchical beam finite elements for geometrically nonlinear analysis coupled with asymptotic numerical method. Mech Adv Mater Struct 2021;28(24):2487–500.
[29] Hui Y, Xu R, Giunta G, De Pietro G, Hu H, Belouettar S, et al. Multiscale CUF-FE2 nonlinear analysis of composite beam structures. Comput Struct 2019;221:28–43.
[30] Hui Y, Bai X, Yang Y, Yang J, Huang Q, Liu X, et al. A data-driven CUF-based beam model based on the tree-search algorithm. Compos Struct 2022;300:116123.
[31] Hui Y, Giunta G, Liu X, Zheng J, Yang J, Huang W, et al. On the coupling of data-driven computing and model-driven computing with CUF-based beam models. Thin- Walled Struct 2024;195:111394.
[32] Carrera E, Pagani A, Petrolo M, Zappino E. A component-wise approach in structural analysis. Computat Methods Eng Sci 2012;4:75–115.
[33] Filippi M, Zappino E, Carrera E, Castaniè B. Effective static and dynamic finite element modeling of a double swept composite rotor blade. J Am Helicopter Soc 2020;65(3):1–12.
[34] Filippi M, Zappino E, Carrera E. Multidimensional models for double-swept helicopter blades. AIAA J 2019;57(6):2609–16.
[35] Pai PF. Highly flexible structures: modeling, computation, and experimentation. Am Inst Aeronaut Astronautics, Reston, VA, 2007.
[36] Pagani A, Carrera E. Unified formulation of geometrically nonlinear refined beam theories. Mech Adv Mater Struct 2018;25(1):15–31.
[37] Carrera E, Filippi M. A refined one-dimensional rotordynamics model with three-dimensional capabilities. J Sound Vib 2016;366:343–56.
[38] Yoo HH, Ryan RR, Scott RA. Dynamics of flexible beams undergoing overall motions. J Sound Vib 1995;181(2):261–78.
[39] Christensen ER, Lee SW. Nonlinear finite element modeling of the dynamics of unrestrained flexible structures. Comput Struct 1986;23(6):819–29.